Materials Science & Engineering A 766 (2019) 138400

Contents lists available at ScienceDirect

Materials Science & Engineering A

journal homepage: www.elsevier.com/locate/msea

# Overcoming the strength-ductility trade-off by the combination of static recrystallization and low-temperature heat-treatment in Co-Cr-W-Ni alloy for stent application

Kosuke Ueki[a,*], Soh Yanagihara[b], Kyosuke Ueda[b], Masaaki Nakai[a], Takayoshi Nakano[c], Takayuki Narushima[b]

[a] Department of Mechanical Engineering, Kindai University, 3-4-1, Kowakae, Higashiosaka, 577-8502, Japan
[b] Department of Materials Processing, Graduate School of Engineering, Tohoku University, 6-6-02, Aza-Aoba, Aramaki, Aoba-ku, Sendai, 980-8579, Japan
[c] Division of Materials Science and Engineering, Graduate School of Engineering, Osaka University, 2-1, Yamada-Oka, Suita, Osaka, 565-0871, Japan

ARTICLE INFO

*Keywords:*
Co-Cr-W-Ni alloy
Static recrystallization
Mechanical properties
Plastic deformation

ABSTRACT

A process combining swaging, static recrystallization, and heat treatment at 873 K (low-temperature heat-treatment, LTHT) was developed for achieving both high ultimate strength and high ductility in Co-20Cr-15W-10Ni (mass%, CCWN) alloy for stent application. The alloys swaged to a sectional area reduction rate of 58.3% were annealed at 1373–1473 K for 30–300 s. Under annealing at 1373 K for 300 s, a fine grain structure with an average grain size of ~6 μm formed, while under annealing at 1473 K, a structure with an average grain size of 12 μm formed after 120 s. In the alloys annealed at 1373–1448 K, the formation of η-phase precipitates ($M_6X$-$M_{12}X$ type, M: metallic elements, X: C and/or N) was observed, while no precipitates were observed in the alloys annealed at 1473 K. The improvement in ultimate strength by grain refinement was confirmed. Alloys annealed at 1473 K showed higher ductility compared to those annealed at 1373–1448 K even if the grain size was similar. It is considered that the η-phase precipitates deteriorated the ductility of the annealed alloys. LTHT suppressed the strain-induced martensitic γ-to-ε transformation to improve the ductility of the fine-grained as well as coarse-grained alloys. Thus, regardless of the grain size, it is newly evidenced that LTHT effectively improves ductility in CCWN alloy. By combining high-temperature short-time annealing and LTHT, both the ultimate strength and ductility of Co-20Cr-15W-10Ni (mass%) alloy improved, and it was possible to provide properties suitable for next-generation balloon-expandable stents with Co-20Cr-15W-10Ni (mass%) alloy.

## 1. Introduction

The Co-20Cr-15W-10Ni (mass%, CCWN) alloy specified by ASTM F90 has excellent mechanical properties and corrosion resistance; therefore, it has been widely used in balloon-expandable stents, which are used in the treatment of cardiovascular diseases [1–4]. Our group has investigated the microstructural changes during heat treatment, mechanical properties, and corrosive properties in biomedical Co-Cr alloys [5–8]. In these studies, we discovered that the mechanical properties (especially ductility) of CCWN [6,7] and Co-28Cr-6Mo (mass %) [8] alloys were improved without sacrificing the corrosion resistance by low-temperature heat-treatment (LTHT) at approximately 873 K. A multi-variant thin ε (hcp)-phase formed during LTHT, and the mechanical properties were improved because the pre-existing thin ε-phase inhibits the progress of the ε-phase formed by strain-induced martensitic transformation [7,8].

In recent years, there has been a demand for reducing the diameter of balloon-expandable stents from the viewpoint of achieving further minimally invasive medical treatment. It is necessary to reduce the strut size of the stent. To realize the reduction of the struts, improvement in both, the ultimate strength and ductility in CCWN alloy, is required. In addition, the yield stress should be as low as possible from the viewpoint of balloon expandability. Li et al. investigated the static recrystallization behavior in the CCWN alloy by conducting cold rolling and annealing [9,10]. They reported that excellent ultimate tensile strength-ductility balance was achieved by forming a bimodal structure in which fine grains and coarse grains are mixed [9,10]. However, although CCWN alloy with a bimodal structure showed excellent ultimate

* Corresponding author.
*E-mail addresses:* ueki@mech.kindai.ac.jp (K. Ueki), soh.yanagihara.q8@dc.tohoku.ac.jp (S. Yanagihara), ueda@material.tohoku.ac.jp (K. Ueda), nakai@mech.kindai.ac.jp (M. Nakai), nakano@mat.eng.osaka-u.ac.jp (T. Nakano), narut@material.tohoku.ac.jp (T. Narushima).

https://doi.org/10.1016/j.msea.2019.138400
Received 20 June 2019; Received in revised form 1 September 2019; Accepted 6 September 2019
Available online 07 September 2019

**Table 1**
Chemical compositions of the ASTM F 90 Co–20Cr–15W–10Ni base alloys used in this study (mass%).

| | Co | Cr | W | Ni | Fe | Mn | C | N |
|---|---|---|---|---|---|---|---|---|
| φ 12.7 (d78) | Bal. | 19.89 | 14.82 | 9.91 | 1.86 | 1.55 | 0.07 | 0.03 |
| φ 28.5 (d207) | Bal. | 20.12 | 14.94 | 9.77 | 1.86 | 1.58 | 0.08 | 0.03 |

strength, the yield stress (or 0.2% proof stress) also increased and the ductility was not sufficient for stent applications [9]. Favre et al. reported the dynamic and static recrystallized behavior of CCWN alloy [1,11]. Favre et al. also reported an increase in the ultimate strength and yield stress, and a decrease in deformability grain refinement in compression testing [1]. Hence, these reports indicate that only by simple grain refinement, it is difficult to simultaneously achieve high ultimate strength and high ductility while maintaining low yield stress.

Our group investigated the effect of LTHT on the microstructure and mechanical properties of CCWN alloy with an average grain size of ~80 μm [6,7]. Considering that the grain size of 80 μm is too large for practical balloon-expandable stents, for which the grain size is 20–30 μm, it is necessary to investigate the effectiveness of LTHT process on CCWN alloy with finer grains. We considered that the process which combined grain refinement using static recrystallization and LTHT was effective. Therefore, this study investigated the static recrystallization behavior of CCWN alloy and the effect of LTHT on mechanical properties in CCWN alloy with a fine grain structure.

## 2. Experimental

### 2.1. Specimen preparation

CCWN alloy bars with diameters of φ28.5 and φ12.7 mm (Carpenter Technology Corporation, PA, USA) were used as the base alloys. The chemical composition of the alloy bars is listed in Table 1. The electron backscatter diffraction (EBSD) inverse pole figure (IPF) maps of the alloys are shown in Fig. 1. The average grain sizes of the φ28.5 and φ12.7 mm base alloys were 207 μm and 78 μm, and referred to as d207 and d78 alloys, respectively. Cold swaging was performed on the d207 alloy, which is referred to as the as-swaged alloy. The cold swaging process was conducted at room temperature (298 K) and the reduction rate of the cross-sectional area in cold swaging was 58.3%. In cold swaging, the jig diameter was reduced from φ28 to φ18 mm (φ28 → φ26 → φ24 → φ22 → φ20 → φ18 mm). Because cracks were observed in the alloy after further swaging, 58.3% swaged alloy was used in this study. The as-swaged alloy was then annealed to investigate the static recrystallization behavior.

**Table 2**
Abbreviation of annealed alloys used in this study.

| Alloys | | Annealing time, *t*/s | | | | |
|---|---|---|---|---|---|---|
| Annealing temperature, *T*/K | | 100 | 120 | 150 | 180 | 300 |
| Base alloy (d78) | | | | | | |
| Base alloy (d207) | 1473 | 1473-d6 | 1473-d12 | | | |
| | 1448 | | 1448-d5 | 1448-d17 | | |
| | 1423 | | 1423-d9 | 1423-d10 | | |
| | 1373 | | | 1373-d3 | 1373-d4 | 1373-d6 |

### 2.2. Heat treatment

The as-swaged alloys were machined into cylindrical shapes with dimensions of φ6.5 mm × 45 mm. The cylindrical specimens were sealed inside $SiO_2$ ampoules under an Ar atmosphere at pressures of 0.02–0.03 MPa to avoid decarburization and/or denitrization during annealing [12,13]. Subsequently, they were placed in an electric-resistance muffle furnace heated to the annealing temperature. The annealing conditions were 1373–1473 K for 30–300 s. After annealing, the cylindrical specimens were water-quenched simultaneously by breaking their $SiO_2$ ampoules.

LTHT was performed on the base alloys (d207 and d78) and annealed alloys. The condition of LTHT was a temperature of 873 K for a holding time of 14.4 ks [6,7]. Focused on the annealing temperature (K) and grain size (μm), the annealed alloys were named as shown in Table 2. In Table 2, the numbers following "d" represent the grain size of the alloys. For example, the 1473-d12 alloy was subjected to annealing at 1473 K and has an average grain size of 12 μm. In addition, the alloys subjected to LTHT were designated as, for example, d207LTHT, d78LTHT, and 1473-d12 LTHT.

### 2.3. Tensile testing

Tensile tests were conducted for the d78, d207, annealed alloys and their LTHT-ed alloys using a mechanical tensile tester (RTF−1325, A&D Company Ltd., Tokyo, Japan). The specimens were machined to have gauge lengths of 10 mm and diameters of 3 mm and then pulled at a nominal strain rate of $1.67 \times 10^{-4}$ $s^{-1}$ at room temperature. After the tensile test, the plastic strain was calculated by measuring displacement of gauge length in the fractured specimens.

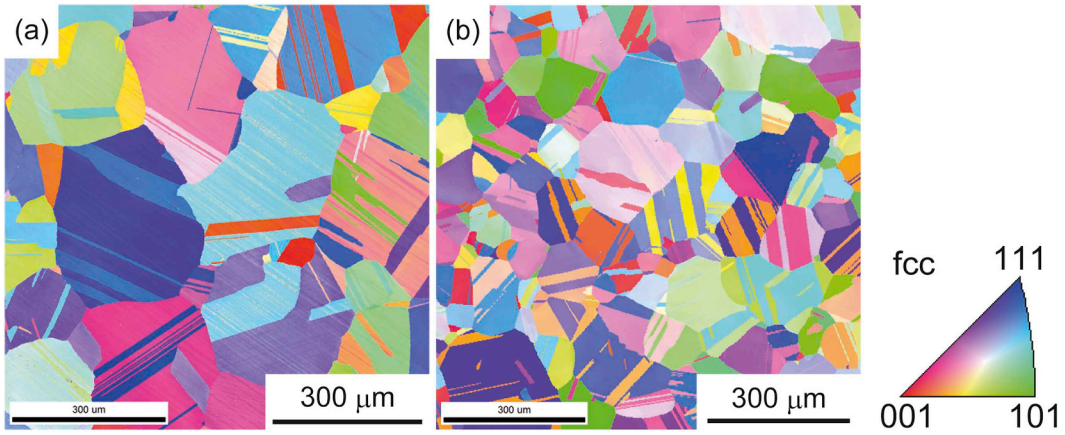


**Fig. 1.** EBSD IPF maps of (a) d207 and (b) d78 base alloys.

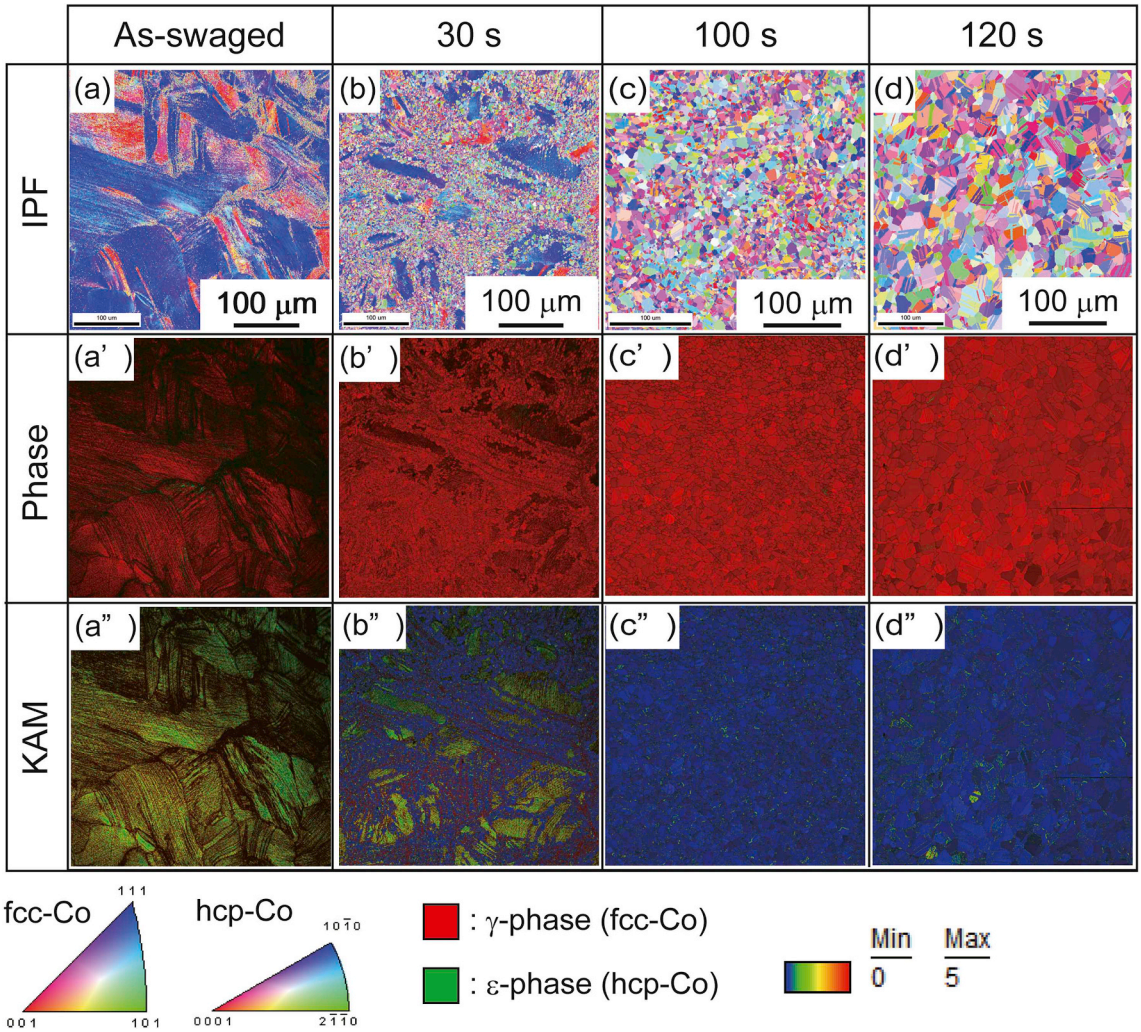


**Fig. 2.** EBSD IPF, phase and KAM maps of (a, a', a") as-swaged alloy and the alloys annealed at 1473 K for (b, b', b") 30 s, (c, c', c") 100 s and (d, d', d") 120 s.

### 2.4. Microstructure observation and analysis

The microstructure of the alloys was observed by scanning electron microscopy-backscattered electron (SEM-BSE, JSM-7800F, JEOL Ltd., Tokyo, Japan) and EBSD. For annealed alloys, the phase of precipitates was analyzed; electrolytic extraction of the alloys was performed at 2 V for 10.8 ks in a $10H_2SO_4$–$90CH_3OH$ (vol%) solution, and the precipitates electrolytically extracted from the alloys were collected as residue after filtering the electrolyte and analyzed by X-ray diffraction (XRD, D8 advance, Bruker AXS K.K., Karlsruhe, Germany) [5,12–14].

### 2.5. In-situ XRD analysis

To analyze the effect of grain size on the behavior of strain induced γ-to-ε martensitic transformation during deformation, in-situ XRD [6,7] was conducted for d207, annealed alloys, and their LTHT-ed alloys. Specimens for in-situ XRD analysis were machined to the shapes with gauge lengths of 13 mm and rectangular cross-sections of 3.5 × 1 $mm^2$. The thin surface oxide layer was removed by mechanical polishing. In addition, the specimens were electrolytically mirror-polished to eliminate the surface damage layer produced by machining and mechanical polishing. Electrolytic polishing was performed at a DC voltage difference of 6 V at 273 K for 60 s in $10H_2SO_4$–$90CH_3OH$ (vol%). To obtain diffracted X-rays from many grains, the XRD measurements were performed while the specimen was being swung.

## 3. Results

### 3.1. Static recrystallization

Fig. 2 shows the EBSD IPF, phase, and kernel average misorientation (KAM) maps of the as-swaged alloy and the alloys annealed at 1473 K for 30–120 s. A homogeneously strained structure was obtained by swaging, as shown in Fig. 2(a"). Even after swaging, almost no strain-induced martensitic transformation occurred, and the matrix of the as-swaged alloy was single γ(fcc)-phase (Fig. 2(a')). In the alloy annealed at 1473 K for 30 s, the KAM value was partially high, suggesting that static recrystallization was not completed. In the alloys annealed at 1473 K for 100 (1473-d6) and 120 s (1473-d12), a fully recrystallized structure was observed. EBSD IPF maps of all the annealed alloys are summarized in Fig. 3. The alloys annealed at 1373–1448 K for 120 s or more have fully recrystallized structures. Fig. 4 shows the average grain size of the annealed alloys. The grain size increased with increasing annealing time. The lower the annealing temperature, the lower the grain growth rate. At an annealing temperature of 1373 K, the average grain size was ~6 μm even after annealing for a relatively long time (300 s). Among the fully recrystallized alloys, 1473-d6, 1473-d12, 1448-d17, 1423-d10, 1373-d3, and 1373-d6 alloys were used for microstructure analysis, LTHT, and mechanical property evaluation.

Fig. 5 shows the XRD patterns of precipitates electrolytically extracted from as-received, as-swaged, 1473-d12, 1448-d17, 1423-d10, and 1373-d6 alloys. No precipitates were detected in both as-received

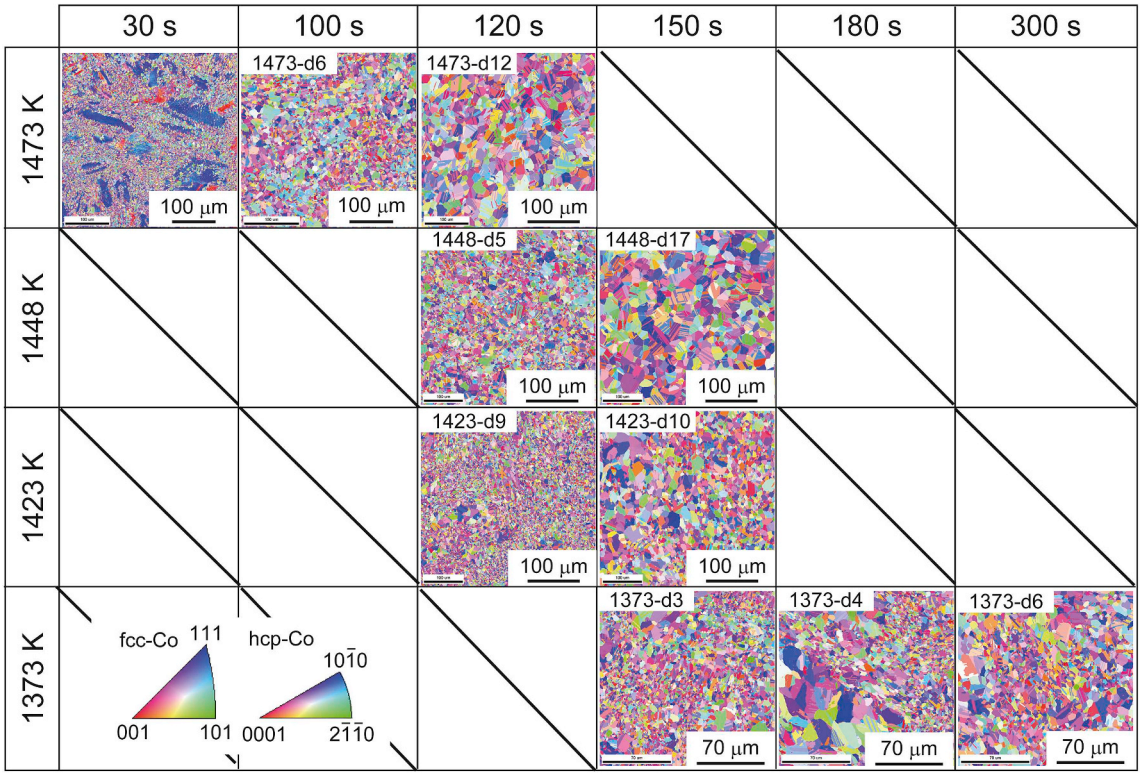


**Fig. 3.** EBSD IPF maps of the alloys annealed at 1373–1473 K for 30–300 s.

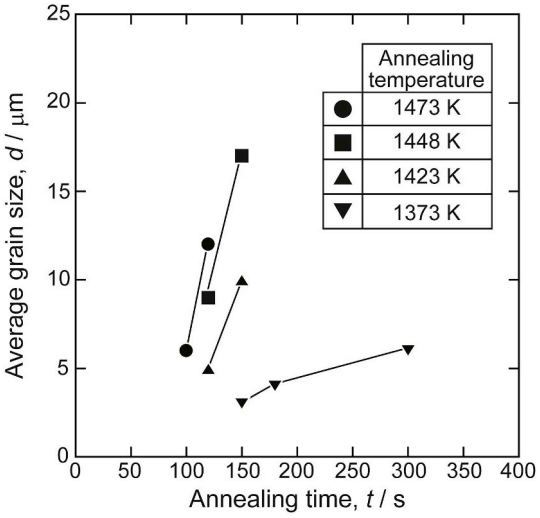


**Fig. 4.** Relationship between average grain size and annealing condition.

and as-swaged alloys. This result confirms that no precipitates were formed during cold swaging. In the 1448-d17, 1423-d10, and 1373-d6 alloys, formation of the η-phase ($M_6X$-$M_{12}X$ type, M: metallic elements, X: C and/or N) was confirmed. The peak intensity of the η-phase increased with decreasing annealing temperature. Fig. 6 (a,b,c) show SEM-BSE images of the alloys for which η-phase peaks were observed in Fig. 5. White particles, which appear to be η-phase, were observed.

Fig. 6 (a',b',c') show SEM images of the precipitates, which were electrolytically extracted from the alloys. The amount of precipitates decreased with increasing annealing temperature. This result was in good agreement with the tendency confirmed from XRD analysis (Fig. 5).

Changes in grain size, precipitate phase, and amount were not observed after LTHT of the annealed alloys with the fine-grained microstructure.

### 3.2. Tensile properties

Fig. 7 shows the 0.2% proof stress and ultimate tensile strength of the annealed and LTHT-ed alloys. The 0.2% proof stress and ultimate tensile strength increased by grain refinement. Fig. 8 shows the plastic elongation of the alloys. Improvement in ductility by LTHT was observed except for 1473-d6. The 1473-d12 LTHT alloy showed excellent strength-ductility balance, with a plastic elongation of ~70% and ultimate tensile strength of ~1200 MPa. The tensile properties of the annealed alloys and their LTHT-ed alloys are summarized in Table 3.

## 4. Discussion

### 4.1. Effect of cold swaging and annealing temperature on static recrystallization

In this study, cold swaging was chosen as the method for applying strain. Compared to cold rolling, cold swaging can produce a homogeneously strained rod-shape specimen. In fact, a significant effect of the measurement position on the average grain size of the annealed alloys was not observed in this study."

As shown in the EBSD IPF maps of Fig. 3, the alloys annealed at high temperature for a relatively long time (120 and 150 s for 1473-d12 and 1448-d17 alloys, respectively) had a homogeneous structure with little variation in the size of each grain. Contrarily, the alloys annealed at low temperature (1423-d10, 1373-d3 and 1373-d6) had an inhomogeneous structure in which coarse and fine grains were mixed. Fig. 9 shows the grain size distribution of 1373-d6 alloy (inhomogeneous structure) and 1448-d17 alloy (homogeneous structure). In Fig. 9, dashed line represents d = 5 μm. In the 1373 d6 alloy, the area fraction of the fine grains (d < 5 μm) was higher than that in the 1448-d17 alloy. In addition, coarse grains (d > 5 μm) certainly existed in the 1373-d6 alloy. Li et al. investigated the static recrystallization behavior of 30 and 50%

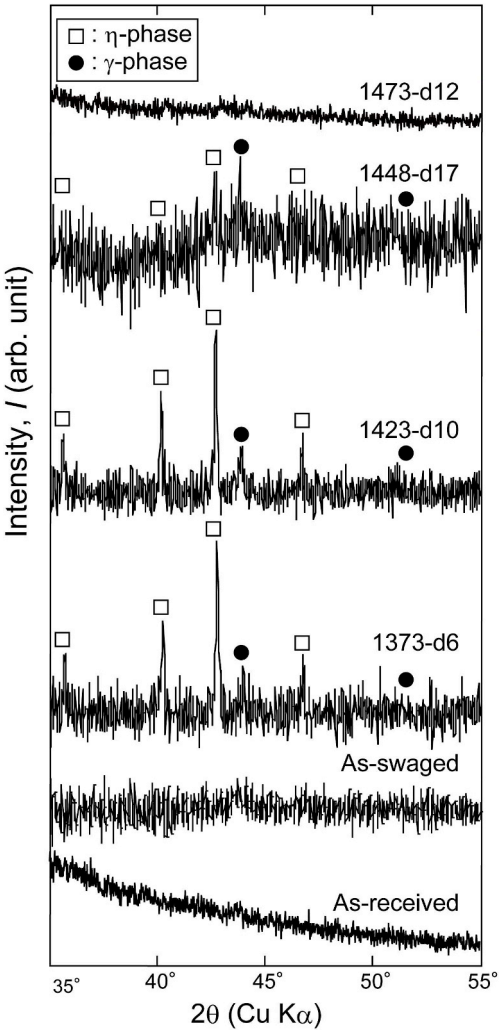


**Fig. 5.** XRD patterns of precipitates electrolytically extracted from as-received, as-swaged, 1373-d6, 1423-d10, 1448-d17 and 1473-d12 alloys.

cold-rolled CCWN alloy by annealing at 1223–1473 K [9,10]. They reported that by annealing at 1223–1373 K for 900 s, a bimodal structure with mixed coarse and fine grains were formed [9]. Although there are differences in the annealing conditions between their study and ours, the results in this study were in good agreement with those reported by Li et al.

Fine η-phase precipitates formed in the alloys annealed at 1373 and 1423 K, which exhibited an inhomogeneous distribution of grain size; moreover, the precipitates were mainly observed at the fine grain area. In our previous studies, the formation of η-phase precipitates was observed in the CCWN alloy heat-treated at 1073–1373 K [6]. The annealing conditions for which the formation of the η-phase precipitates was observed involved higher temperatures and shorter times than those of our previous study [6]. Beltran et al. reported that in the 304 stainless steel, strain accumulation promoted the precipitation of carbides during aging [15,16]. Therefore, in the as-swaged alloy, precipitation was considered to occur at lattice defects caused by cold swaging, such as dislocations and stacking faults in the initial stage of annealing. In addition, during annealing, grain and/or twin boundaries are known to become nucleation sites for precipitates [17,18]. Based on these reports, the as-swaged alloy was more likely to form η-phase precipitates during the annealing process as compared to the unstrained alloy, and it was considered that in this study, η-phase precipitates were formed during annealing from 1373 to 1448 K. There are a few reports that nanometer-order fine precipitates developed during the hot working of the steels impeded recrystallization [19,20]. Kubota et al. reported that suppression of recrystallization could be expected when a large amount of fine precipitates were present [19]. Therefore, it was considered that the bimodal-like inhomogeneous grain size structure was formed because recrystallization and grain growth were partially delayed by fine precipitates.

### 4.2. Effect of annealing temperature on tensile properties

Fig. 10 shows the relationship between the grain size and 0.2% proof stress. The results in this study satisfied the Hall-Petch relationship. If the grain size is equal, no significant influence of annealing temperature on strength is expected. However, in terms of the ductility, alloys annealed at 1473 K show a higher ductility than those annealed at 1373–1448 K even if the grain size is almost equal (see in Fig. 8). In our previous study, the influence of η-phase precipitation on the mechanical properties of CCWN was investigated in detail, and the plastic elongation of the alloy was deteriorated by the formation of η-phase precipitates [6]. Teague et al. [21] and Gupta et al. [22] also reported a deterioration in the ductility by the formation of the η-phase. From these results, we conclude that the deterioration in the ductility with decreasing annealing temperature was due to the precipitation of the η-phase during annealing.

### 4.3. Grain size dependence of plastic deformation behavior

True stress-true strain curves and work hardening rate curves of the d207, 1473-d12, 1373-d6 and their LTHT-ed alloys are shown in Fig. 11. The work hardening rate of the d207 and d207LTHT alloys increased with increasing strain in the initial to middle stage of plastic deformation. In contrast, although the 1473-d12 and 1373-d6 and their LTHT-ed alloys showed high work hardening rates in the initial stage of plastic deformation, the work hardening rates gradually decreased with increasing strain. Therefore, it was considered that there is a difference in the microstructure change behavior during plastic deformation between fine and coarse grain structures. Lemy and Pineau investigated the relationship between the stacking fault energy (SFE) and deformation mode of a Co-Cr type alloy [23]. They reported that both, strain-induced martensitic transformation and deformation twinning occurred in the alloy with a SFE of 10–20 mJ· $m^{-2}$, deformation twinning mainly occurred in the alloy with a SFE of 20–30 mJ· $m^{-2}$, both deformation twinning and dislocation slip occurred in the alloy with SFE of 30–50 mJ· $m^{-2}$, and only dislocation slip occurred in the alloy with SFE of more than 50 mJ· $m^{-2}$. The SFE of Co-20Cr-15W-10Ni (mass%) alloy at 250–300 K (near room temperature) was calculated using Thermo-calc (TCFE ver. 9), and the value of SFE near room temperature was ~25 mJ $m^{-2}$. This value was slightly higher than the SFE at which both strain-induced martensitic transformation and deformation twinning occur. However, since these SFEs do not consider the grain size of the alloy and the plastic deformation mechanism was reported to depend on the grain size [24], the possibility that both strain-induced martensitic transformation and deformation twinning occur cannot be denied even in the CCWN alloy.

To clarify the effect of grain refinement and LTHT on strain-induced γ-to-ε martensitic transformation behavior, in-situ XRD analysis and EBSD analysis were conducted. Fig. 12 shows the relationship between the ε-phase fraction ($f_\varepsilon$) and the amount of applied strain in in-situ XRD analysis. The value of $f_\varepsilon$ was calculated from peak intensity of the in-situ XRD patterns using equations (1) and (2) [25]:

$$f_\gamma = I_{\gamma\{200\}} / (I_{\gamma\{200\}} + 1.5 I_{\varepsilon\{10\text{-}10\}}) \quad (1)$$

$$f_\varepsilon = 1 - f_\gamma \quad (2)$$

where, $I_{\gamma\{200\}}$ and $I_\varepsilon$ are the peak intensities for {200} of the γ-phase and {10-10} of the ε-phase, respectively, and $f_\gamma$ is the γ-phase fraction. In the d207 alloy, the ε-phase formed in the middle stage of plastic

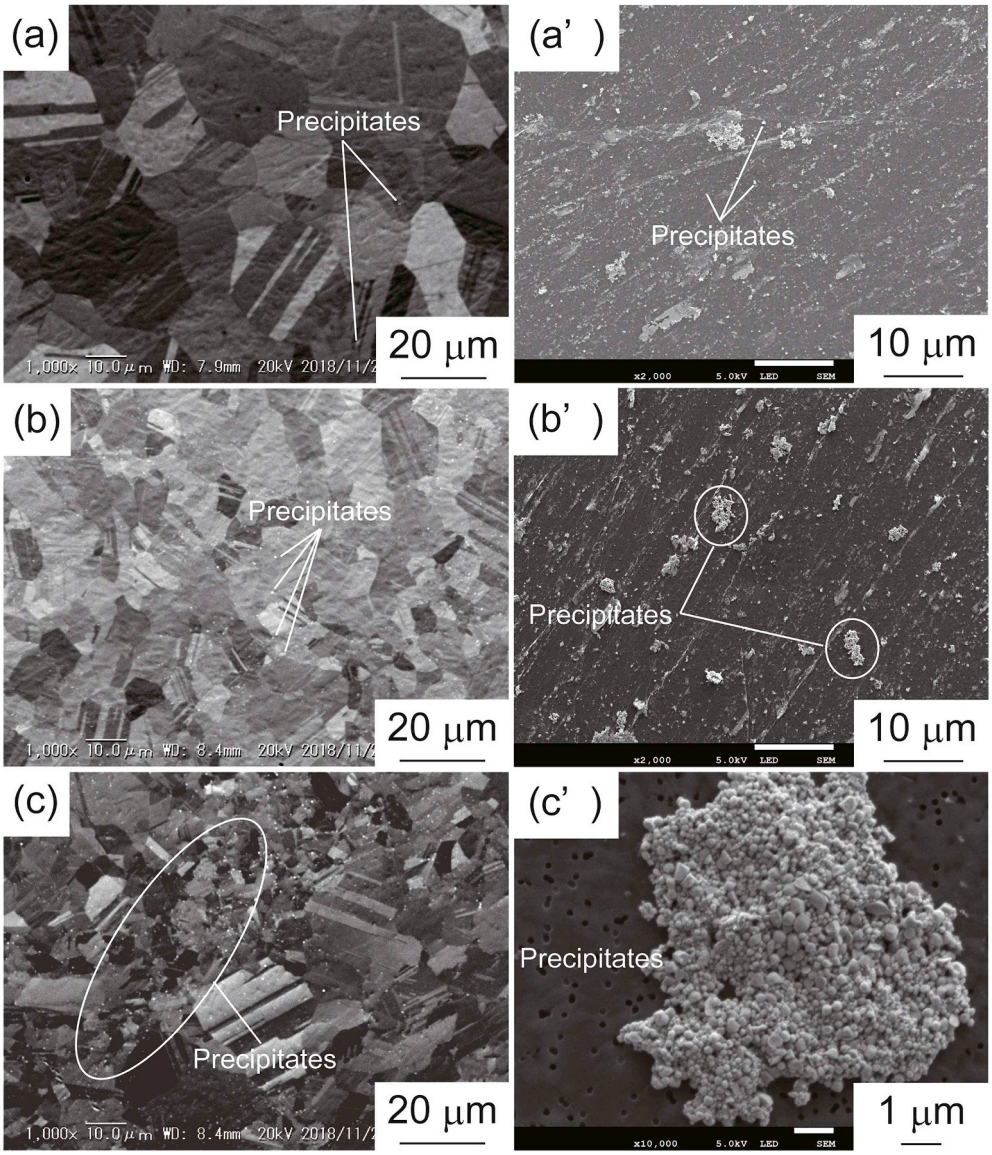


**Fig. 6.** SEM-BSE images of (a) 1448-d17, (b) 1423-d10 and (c) 1373-d6 alloys and SEM images of precipitates electrolytically extracted from (a') 1448-d17, (b') 1423-d10 and (c') 1373-d6 alloys.

deformation (strain: 32%), whereas the d207LTHT alloy maintained a single γ-phase structure during plastic deformation. In the 1473-d12 alloy, the ε-phase formed in the middle stage of plastic deformation (strain: 23%), while in the 1473-d12 LTHT alloy, no ε-phase was formed up to high strained region (strain: ~40%). From these results, it was considered that the strain-induced γ-to-ε martensitic transformation was suppressed by performing LTHT, resulting in the improvement of ductility.

Focusing on the influence of grain size on the ε-phase formation behavior during plastic deformation, in the high strain region, $f_\varepsilon$ of the d207 alloy was higher than that of the 1473-d12 alloy. This trend did not change after LTHT. In transformation-induced plasticity (TRIP) steels and Co-Cr-Mo alloys, there are some reports that the formation of the ε-phase by strain-induced martensitic transformation is suppressed due to grain refinement [26–28]. In addition, Lee et al. proposed an apparent SFE taking into account the austenite grain size in Fe-Mn alloys, and reported an apparent SFE increase with decreasing austenite grain size [29]. The higher SFE, the more stable the γ-phase. Therefore, it was considered that strain-induced γ-to-ε martensitic transformation is suppressed by grain refinement. However, according to the results in this study, the alloy with a fine grain structure showed a higher $f_\varepsilon$ value than the alloy with a coarse grain structure. In order to clarify the mechanism for this phenomenon, microstructure analysis focusing on the formation site of the strain-induced ε-phase was conducted. Fig. 13 shows the EBSD IPF and phase maps of the fractured specimens of the d207, d12, and their LTHT-ed alloys. $f_\varepsilon$ of the 1473-d12 alloy was higher than that of the d207 alloy. No significant difference in $f_\varepsilon$ was observed between d207 and d207 LTHT. However, comparing the 1473-d12 alloy with the 1473-d12 LTHT alloy, the formation of ε-phase due to strain-induced martensitic transformation was suppressed by LTHT. This result was in good agreement with that of in-situ XRD analysis (Fig. 12). Fig. 14 shows the high-magnification EBSD IPF and phase maps of the 1473-d12 alloy. The ε-phase was mainly formed at the grain boundary (GB) and twin boundary (TB). These results suggested that the 1473-d12 alloy showed a higher $f_\varepsilon$ value compared to d207 because the amount of GB and TB (nucleation site of strain-induced ε-phase) increased by grain refinement.

The values of $f_\varepsilon$ calculated from EBSD analysis are lower than those from in-situ XRD analysis. The values of $f_\varepsilon$ by the EBSD analysis were calculated at the inside of a rod-shape tensile test specimens, while those of $f_\varepsilon$ by the in-situ XRD analysis were calculated at the surface of the plate-shape tensile test specimens. If the geometry of the tensile test

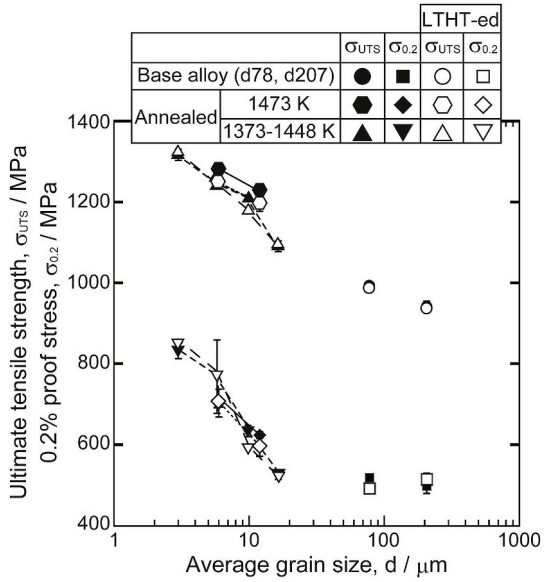


**Fig. 7.** Effect of grain refinement and LTHT on the ultimate tensile strength and 0.2% proof stress of CCWN alloy.

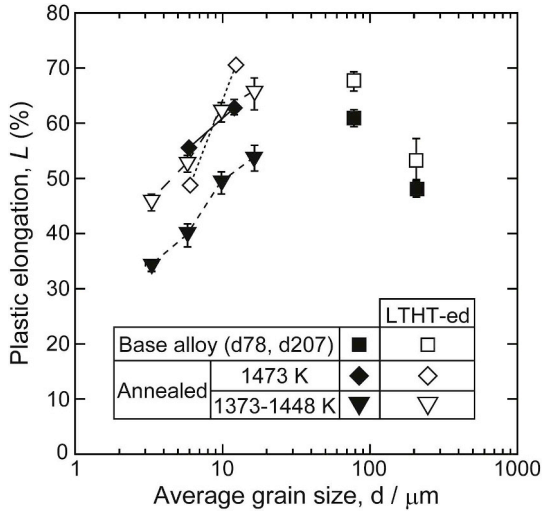


**Fig. 8.** Effect of grain refinement and LTHT on the plastic elongation of CCWN alloy.

**Table 3**
Ultimate tensile strength, 0.2% proof strength and plastic elongation of the annealed alloys and their LTHT-ed alloys.

| Specimen | $\sigma_{UTS}$ (MPa) | $\sigma_{0.2}$ (MPa) | $L$ (%) |
|---|---|---|---|
| d207 | 943 | 499 | 48 |
| d207LTHT | 940 | 486 | 58 |
| d78 | 995 | 520 | 61 |
| d78LTHT | 986 | 490 | 68 |
| 1373-d4 | 1319 | 833 | 34 |
| 1373-d4LTHT | 1325 | 844 | 46 |
| 1373-d6 | 1245 | 697 | 40 |
| 1373-d6LTHT | 1256 | 766 | 53 |
| 1423-d10 | 1211 | 635 | 49 |
| 1423-d10LTHT | 1176 | 588 | 62 |
| 1448-d17 | 1092 | 526 | 54 |
| 1448-d17LTHT | 1096 | 520 | 65 |
| 1473-d6 | 1279 | 704 | 55 |
| 1473-d6LTHT | 1244 | 705 | 49 |
| 1473-d12 | 1227 | 613 | 63 |
| 1473-d12LTHT | 1195 | 592 | 71 |

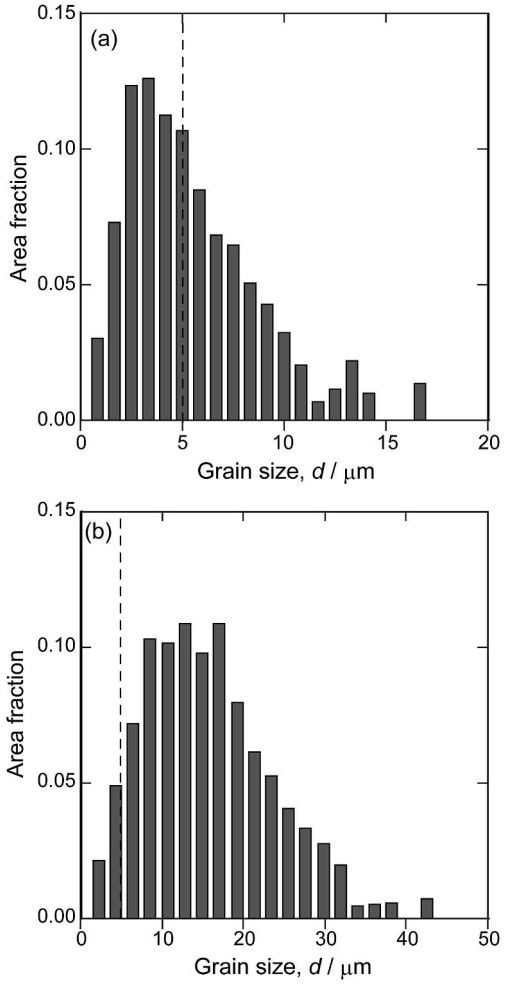


**Fig. 9.** Grain size distribution of (a) 1373-d6 and (b) 1448-d17 alloys (dashed line represents d = 5 μm).

specimens is different, the strain distribution during plastic deformation is also different [30]. The cross-sectional areas of the rod-shape specimens (for tensile test and EBSD) and the plate-shape specimens (for in-situ XRD) are 7.1 $mm^2$ and 3.5 $mm^2$, respectively. In the case of tensile deformation, larger the cross-sectional area, smaller is the local strain at the specimen surface [30]. Therefore, the local strain at the surface of

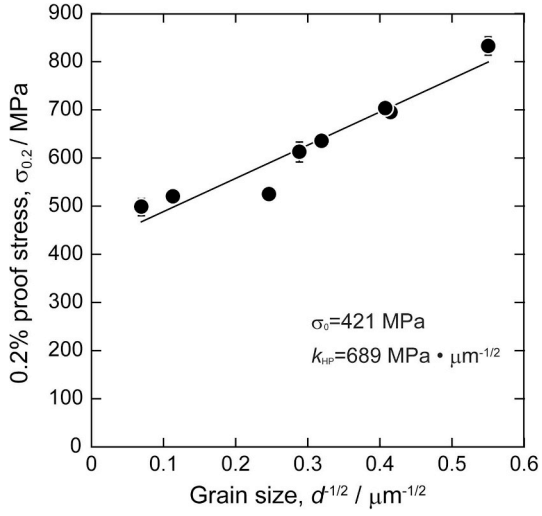


**Fig. 10.** 0.2% proof stress–grain size relationship of the recrystallized alloys.

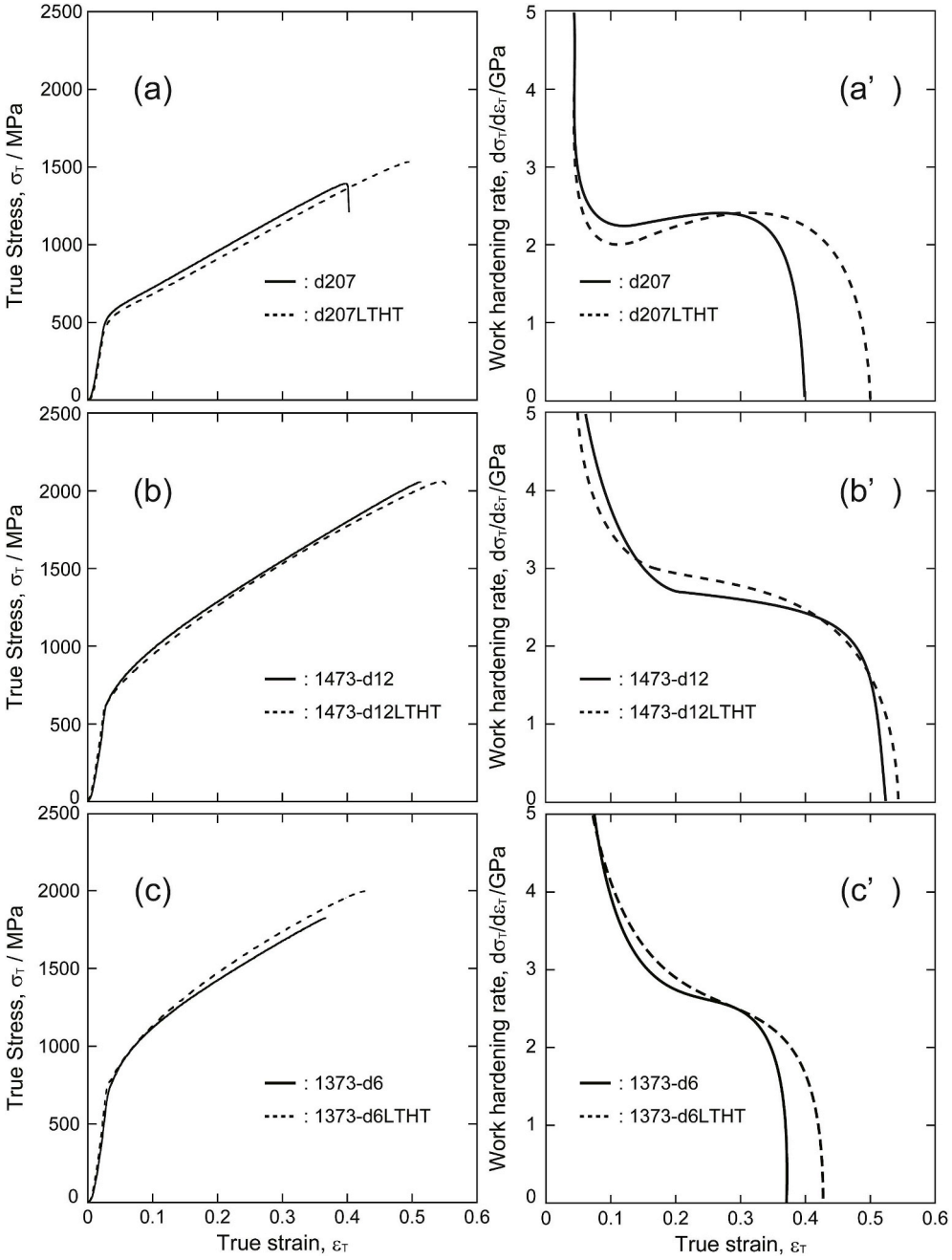


**Fig. 11.** (a, b, c) True stress – true strain curves and (a', b', c') work-hardening rate curves of (a, a') d207 and d207LTHT, (b, b') 1473-d12 and 1473-d12 LTHT and (c, c') 1373-d6 and 1373-d6 LTHT alloys.

the in-situ XRD specimen was considered to be larger than that of tensile test specimen. In other words, during plastic deformation, the plate-shape specimens was considered to have a higher ε-phase fraction than rod-shape specimens.

It is known that specimen geometry also affects elongation. According to Barba's law, the elongation in the tensile test is proportional to the square root of the cross-sectional area [31]. Thus, the elongation of the rod-shape specimens was higher than that of the plate-shape specimens.

Focusing on deformation twinning behavior, Gutierrez-Urrutia et al. reported the deformation twinning stress was empirically proportional to the-1/2 power of grain size and they proposed Eq. (3) [32]:

$$\tau_{tw} = \frac{\gamma}{b} + \frac{K_{tw}^{H-P}}{\sqrt{D}} \quad (3)$$

where γ is the SFE, $b$ is the amplitude of Burgers vector, $K_{tw}^{H\text{-}P}$ is the Hall-Petch constant of twinning and D is the grain size. Eq. (3) shows deformation twinning stress decreases with increasing grain size. That is, it was considered that d207 alloys are easier to form deformation twins than 1473-d12 and 1373-d6 alloys. From these results, there is a possibility in the d207 and d207LTHT alloys that deformation twinning occurred preferentially to strain-induced martensitic transformation, and the increase of work-hardening rate in the initial to middle stage of plastic deformation is due to deformation twinning.

### 4.4. Mechanical properties for next generation balloon-expandable stent

In this study, we achieved the improvement of both ultimate strength and ductility of the CCWN alloy by combining grain refining by static recrystallization and LTHT. Fig. 14 shows the mechanical

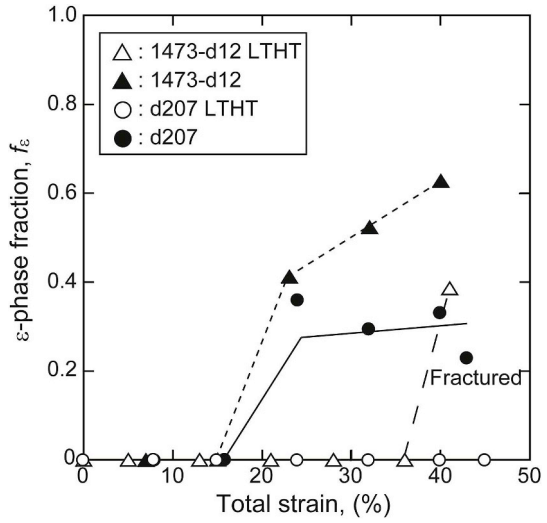


**Fig. 12.** Relationship between ε-phase fractions calculated from In-situ XRD peak intensity ratio and strain of the d207, 1473-d12 and their LTHT-ed alloys.

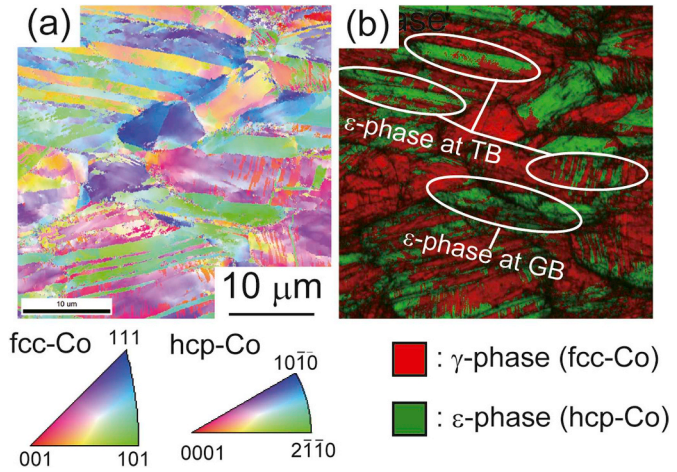


**Fig. 14.** High-magnification EBSD IPF and phase maps of fractured specimen of 1473-d12 alloy.

properties of CCWN alloy reported from other groups and this study. The horizontal axis in Fig. 15 shows elongation, the vertical axis in Fig. 15(a) shows 0.2% proof stress and the vertical axis in Fig. 15(b) shows ultimate tensile strength of the alloys. In addition, the gray area in Fig. 15 represents our target area for the mechanical properties of next-generation balloon-expandable stent; the target values of 0.2% proof stress, ultimate tensile strength, and elongation are set at < 600 MPa, > 1200 MPa, and > 60%, respectively. Teague et al. investigated the effect of long-term heat-treatment on the microstructure and mechanical properties of CCWN alloy [21]. Although the elongation reported by Teague et al. was higher than that of other groups, the ultimate tensile strength was lower than the target value [21]. Li et al. fabricated the CCWN alloy which had the bimodal structure and that alloy showed excellent ultimate tensile strength [9]. However, the 0.2% proof stress of that alloy was also high (804 MPa) and elongation was not sufficient (~45%) for stent application [9]. Compared to these reported mechanical properties, it is newly evidenced that 1473-d12 LTHT alloy has an excellent balance of ultimate strength and ductility, and the increase of 0.2% proof stress due to grain refinement can be minimized. From these results, it was considered that a process combining grain refinement by static recrystallization at high temperatures and LTHT can impart mechanical properties suitable for next generation balloon-expandable stent to CCWN alloy.

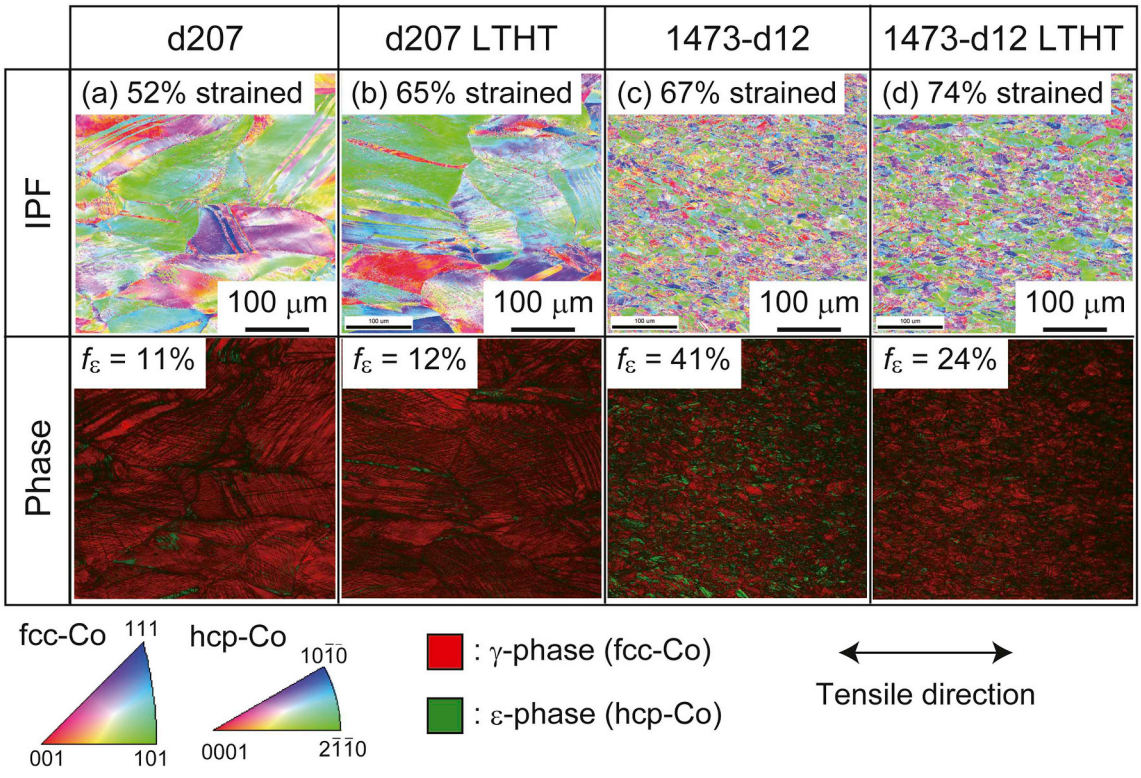


**Fig. 13.** EBSD IPF and phase maps of fractured specimens of (a) d207, (b) d207LTHT, (c) 1473-d12 and (d) 1473-d12 LTHT alloys.

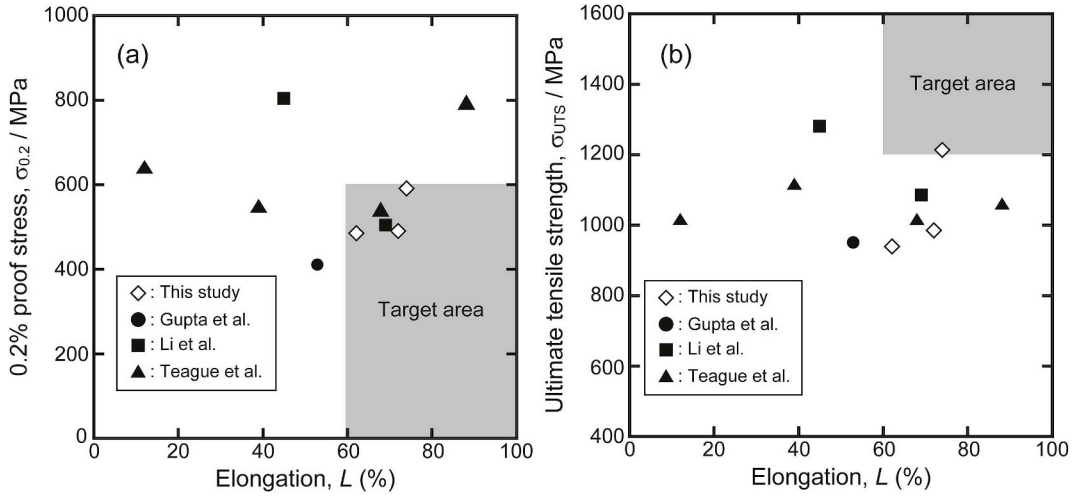


**Fig. 15.** Mechanical properties of CCWN alloys reported by other groups and this study (gray area shows target mechanical properties of base material for next generation stents).

## 5. Conclusions

Co-Cr-W-Ni alloy was processed by cold swaging and annealing, and the effect of grain size and low-temperature heat treatment (LTHT) on the microstructure and mechanical properties of the alloys was investigated.

(1) In the alloy annealed at 1373–1448 K, the formation of η-phase precipitates was observed, while no η-phase was observed in the alloy annealed at 1473 K. The amount of η-phase increased with decrease of the annealing temperature. By annealing at 1373–1448 K, the nanoscale η-phase formed, and these η-phase precipitates inhibited the progress of static recrystallization and grain growth, which formed the bimodal-like inhomogeneous structure consisting of both coarse and fine grains.
(2) The alloy annealed at 1473 K showed higher ductility than the alloys annealed at 1373–1448 K. This is because η-phase precipitates developed and deteriorated the ductility of the alloys.
(3) In the fully recrystallized specimens, the ductility increased ~10% by LTHT regardless of the grain size. In particular, the 1473-d12 LTHT alloys showed high plastic elongation and high ultimate tensile strength (~70% and ~1200 MPa, respectively). The usefulness of LTHT on the alloy ductility was demonstrated not only for coarse grain structure but also for fine grain structure. By combining grain refinement using static recrystallization by high temperature annealing and LTHT, both the high ultimate strength and high ductility of the Co-Cr-W-Ni alloy were achieved, which can be utilized for next-generation stents.

## Data availability

The raw/processed data required to reproduce these findings cannot be shared at this time as the data also forms part of an ongoing study.

## Acknowledgments

This study was financially supported by the Japan Society for the Promotion of Science KAKENHI [Grant number: JP 16J04279, 18H05254].

## References

[1] J. Favre, Y. Koizumi, A. Chiba, D. Fabregue, E. Maire, Deformation behavior and dynamic recrystallization of biomedical Co-Cr-W-Ni (L-605) alloy, Metall. Mater. Trans. A 44 (2013) 2819–2830.
[2] P. Poncin, J. Proft, "Stent tubing: understanding the desired attributes", med. Device mater, Proc. Mater. Processes Med. Devices Conf. (2003) 253–259.
[3] F.R. Morral, Cobalt alloys as implants in humans, J. Mater. 1 (1966) 384–412.
[4] R.V. Marrey, R. Butgermeister, R.B. Grishaber, R.O. Ritchie, Fatigue and life prediction for cobalt-chromium stents: a fracture mechanics analysis, Biomaterials 27 (2006) 1988–2000.
[5] T. Narushima, S. Mineta, Y. Kurihara, K. Ueda, Precipitates in biomedical Co-Cr alloys, JOM 65 (2013) 489–504.
[6] K. Ueki, K. Ueda, T. Narushima, Microstructure and mechanical properties of heat-treated Co-20Cr-15W-10Ni alloy for biomedical application, Metall. Mater. Trans. A 47 (2016) 2773–2782.
[7] K. Ueki, K. Ueda, M. Nakai, T. Nakano, T. Narushima, Microstructural changes during plastic deformation and corrosion properties of biomedical Co-20Cr-15W-10Ni alloy heat-treated at 873 K, Metall. Mater. Trans. A 49 (2018) 2393–2404.
[8] K. Ueki, M. Abe, K. Ueda, M. Nakai, T. Nakano, T. Narushima, Synchronous improvement in strength and ductility of biomedical Co-Cr-Mo alloys by unique low-temperature heat treatment, Mater. Sci. Eng. A 739 (2019) 53–61.
[9] C.L. Li, C.H. Park, S.W. Choi, S.W. Lee, J.K. Hong, J.T. Yeom, High strength and high ductility in the Co-20Cr-15W-10Ni alloy having a bimodal grain structure achieved by static recrystallization, Mater. Sci. Eng. A 732 (2018) 70–77.
[10] C.L. Li, J.M. Oh, J.T. Yeom, C.H. Park, Bimodal grain-structure formation in a Co-Cr-based superalloy during ultrahigh-homologous temperature annealing without severe plastic deformation, J. Alloys Compd. 783 (2019) 173–178.
[11] J. Favre, D. Fabregue, E. Maire, A. Chiba, Grain growth and static recrystallization kinetics in Co-20Cr-15W-10Ni(L-605) cobalt-base superalloy, Philos. Mag. 94 (2014) 1992–2008.
[12] S. Mineta, Alfirano, S. Namba, T. Yoneda, K. Ueda, T. Narushima, Metall. Mater. Trans. A 43 (2012) 3351–3358.
[13] S. Mineta, S. Namba, T. Yoneda, T. Ueda, T. Narushima, Carbide formation and dissolution in biomedical Co-Cr-Mo alloys with different carbon contents during solution treatment, Metall. Mater. Trans. A 41 (2010) 2129–2138.
[14] K. Ueki, Y. Kurihara, S. Mineta, Alfirano, K. Ueda, S. Namba, T. Yoneda, T. Narushima, Changes in microstructure of biomedical Co-Cr-Mo alloys during aging at 973 to 1373 K, Mater. Trans. 57 (2016) 2048–2053.
[15] R. Beltran, E.A. Trillo, R.J. Romero, L.E. Murr, A.H. Advani, W.W. Fisher, Combined effects of strain and grain size on carbide precipitation and sensitization in 304 stainless steel, Scr. Metall. Mater. 30 (1994) 1021–1025.
[16] R. Beltran, J.G. Maldonado, L.E. Murr, W.W. Fisher, Effects of strain and grain size on carbide precipitation and corrosion sensitization behavior in 304 stainless steel, Acta Mater. 45 (1997) 4351–4360.
[17] H.U. Hong, B.S. Rho, S.W. Nam, Correlation of the M23C6 precipitation morphology with grain boundary characteristics in austenitic stainless steel, Mater. Sci. Eng. A 318 (2001) 285–292.
[18] E.A. Trillo, L.E. Murr, A TEM investigation of M23C6 carbide precipitation behaviour on varying grain boundary misorientations in 304 stainless steels, J. Mater. Sci. 33 (1998) 1263–1271.
[19] I. Weiss, J.J. Jonas, Interaction between recrystallization and precipitation during

the high temperature deformation of HSLA steels, Metall. Trans. A 10A (1979) 831–640.
[20] M. Kubota, Y. Kobayashi, K. Ushioda, J. Takahashi, Effect of carbon content on static recrystallization behavior of work-hardened austenite in low alloy steel and its mechanism, Mater. Trans. 58 (2017) 196–205.
[21] J. Teague, E. Cerreta, M. Stout, Metall. Mater. Trans. A, "Tensile properties and microstructure of Haynes25 alloy after aging at elevated temperatures for extended times", Metall. Mater. Trans. A 35 (2004) 2767–2781.
[22] R.K. Gupta, M.K. Karthikeyan, D.N. Bhalia, B.R. Ghosh, P.P. Sinha, Effect of microstructure on mechanical properties of refractory Co-Cr-W-Ni alloy, Met. Sci. Heat Treat. 50 (2008) 175–179.
[23] L. Rémy, Pineau, Twinning and strain-induced f.c.c.→h.c.p. transformation on the mechanical properties of Co Ni Cr Mo alloys, Mater. Sci. Eng. 26 (1976) 123–132.
[24] M. Sage, C. Guillaud, Méthode d'analyse quantitative des variétés allotropiques du cobalt par les rayons X, Rev. Métall. 47 (1950) 139–145.
[25] M.-M. Wang, C.C. Tasan, D. Ponge, A. Kostka, D. Raabe, Smaller is less stable: size effects on twinning vs. transformation of reverted austenite in TRIP-maraging steels, Acta Mater. 79 (2014) 268–281.
[26] S. Takaki, H. Nakatsu, Y. Tokunaga, Effects of austenite grain size on ε martensitic transformation in Fe-15mass%Mn alloy, Mater. Trans. 34 (1993) 489–495.
[27] T. Iwamoto, T. Tsuta, Computational simulation of the dependence of the austenitic grain size on the deformation behavior of TRIP steels, Int. J. Plast. 16 (2000) 791–804.
[28] P. Huang, H.F. López, Strain induced ε-martensite in a Co-Cr-Mo alloy: grain size effects, Mater. Lett. 39 (1991) 244–248.
[29] Y.K. Lee, C.S. Choi, Driving force for γ→ε martensitic transformation and stacking fault energy of γ in Fe-Mn binary system, Metall. Mater. Trans. A 31A (2000) 355–360.
[30] Y.H. Zhao, Y.Z. Guo, Q. Wei, A.M. Dangelewicz, C. Xu, Y.T. Zhu, T.G. Langdon, Y.Z. Zhou, E.J. Lavernia, Influence of specimen dimensions on the tensile behavior of ultrafine-grained Cu, Scr. Mater. 59 (2008) 627–630.
[31] Y. Takeda, C. Kiattisaksri, M. Aramaki, S. Munetoh, O. Furukimi, Effects of specimen thickness in tensile tests on elongation and deformation energy for industrially pure iron, ISIJ Int. 57 (2017) 1129–1137.
[32] I.G. Urrutia, S. Zaefferer, D. Raabe, The effect of grain size and grain orientation on deformation twinning in a Fe-22wt.%Mn-0.6wt.%C TWIP steel, Mater. Sci. Eng. A 527 (2010) 3552–3560.